Evolution of E × B shear and coherent fluctuations prior to H-L transitions in DIII-D and control strategies for H-L transitions

D. Eldon,[1,2,a)] R. L. Boivin,[3] C. Chrystal,[4] R. J. Groebner,[3] G. R. McKee,[5] L. Schmitz,[6] G. R. Tynan,[2] Z. Yan,[5] J. A. Boedo,[2] K. H. Burrell,[3] J. D. King,[3] E. Kolemen,[1] N. C. Luhmann, Jr.,[7] C. M. Muscatello,[3] T. H. Osborne,[3] and P. B. Snyder[3]
[1]*Princeton University, Princeton, New Jersey 08543, USA*
[2]*University of California San Diego, 9500 Gilman Drive, La Jolla, California 92093-0417, USA*
[3]*General Atomics, P.O. Box 85608, San Diego, California 92186-5608, USA*
[4]*Oak Ridge Associated Universities, 1299 Bethel Valley Road, Building SC-200, Oak Ridge, Tennessee 37830, USA*
[5]*University of Wisconsin-Madison, Madison, Wisconsin 53706, USA*
[6]*University of California Los Angeles, P.O. Box 957099, Los Angeles, California 90095-7099, USA*
[7]*University of California Davis, University of California Davis, 347 Memorial Union, Davis, California 95616, USA*

(Received 28 July 2015; accepted 12 October 2015; published online 19 November 2015)

While operating a magnetic fusion device in H-mode has many advantages, care must be taken to understand and control the release of energy during the H-L back transition, as the extra energy stored within the H-mode transport barrier will have the potential to cause damage to material components of a large future tokamak such as ITER. Examining a scenario where the H-L back transition sequence begins before the $E \times B$ shearing layer decays on its own, we identify a long-lived precursor mode that is tied to the events of the H-L sequence and we develop a robust control strategy for ensuring gradual release of energy during the transition sequence. Back transitions in this scenario commonly begin with a rapid relaxation of the pedestal, which was previously shown to be inconsistent with ideal peeling-ballooning instability as the trigger [Eldon *et al.*, Phys. Plasmas **22**, 052109 (2015)], despite being otherwise similar to a large type-I Edge Localized Mode (ELM). This so-called transient occurs when the $E \times B$ shearing rate $\omega_{E\times B}$ is significantly larger than the turbulence decorrelation rate ω_T, indicating that this is not the result of runaway turbulence recovery. The transient is always synchronous with amplitude and propagation velocity modulations of the precursor mode, which has been dubbed the Modulating Pedestal Mode (MPM). The MPM is a coherent density fluctuation, which, in our scenario at least, reliably appears in the steep gradient region with $f \approx 70\,\mathrm{kHz}$, $k_\theta \approx 0.3\,\mathrm{cm}^{-1}$, and it exists for $\gtrsim 100\,\mathrm{ms}$ before the onset of back transitions. The transient may be reliably eliminated by reducing toroidal rotation in the co-current direction by the application of torque from counter-injecting neutral beams. The transient in these "soft" H-L transitions is then replaced by a small type-III ELM, which is also always synchronous with the MPM, and MPM shows the same behavior in both hard and soft cases. © *2015 AIP Publishing LLC*. [http://dx.doi.org/10.1063/1.4935919]

I. INTRODUCTION

High confinement mode (H-mode) is an attractive regime for tokamak reactor operation as it allows higher temperature, density, and confinement time than L-mode or Ohmic operation.[2,3] In H-mode, additional stored energy builds up inside a transport barrier that is present at the outer edge of the plasma, in the last ≈5% of closed flux surfaces. During the termination phase of H-mode discharges, the transition back to L-mode is often led by a transient spike in D_α emission and rapid relaxation of the edge pressure profile, which is superficially similar to a large type-I ELM. This occurs even in shots that are specifically constructed to produce a long "dithering" phase between ELM-free H-mode and L-mode;[4,5] that is, even slow transition sequences are observed to include sudden drops in stored energy in addition to an otherwise gradual decay of energy. This is a problem because rapid pedestal relaxations are expected to cause severe heat loads on plasma facing components in ITER.[6–9] Although the D_α spike and pedestal reduction at the start of many H-L sequences are similar to the results of a large type-I ELM, and this event has been referred to as a type-I ELM in other work related to H-L back transitions,[5] it has been shown previously that the triggering mechanism is different: type-I ELMs result from ideal peeling-ballooning instability,[10,11] whereas these H-L back transition transients do not.[1] This means that attempts to predict heat loads for these transients cannot take advantage of work that has been done to develop scaling relations for ELM power deposition[12] nor are ELM suppression techniques[13] likely to be effective.

Previous experiments have developed a scenario that produces an intermediate confinement regime or "I-phase" between L and H-mode and have used this to study L-H and H-L transition physics.[4,5] Results from these experiments indicate that I-phase is consistent with a predator prey interaction between zonal flows and turbulence,[14,15] and this predator prey theory offers an explanation of essential L-H

a)Electronic mail: deldon@princeton.edu

transition physics. However, the large initial transient appears at the start of H-L back transition sequences and breaks the symmetry between L-I-H and H-I-L transition sequences, complicates efforts to understand H-L transitions, and interferes with the "soft landing," which might otherwise be allowed by the H-I-L back transition sequence.[16]

Working in the scenario of Schmitz *et al.*[5] (which produces I-phase as described above), with experimental setup described in Section II, we seek understanding of the physical nature of the transient and a means to limit the amount of energy it releases and pursue this in three investigations. First, we test whether the initiation of the H-L sequence is consistent with spontaneous decay and collapse of the transport barrier (due to insufficient power), by tracking evolution of the $E \times B$ shearing rate $\omega_{E\times B}$ in comparison to the decorrelation rate of turbulence ω_T. The hypothesis that the transport barrier collapses on its own is described in more detail in Section III A, and the results are presented in Section III B. The results show that activity associated with the H-L transition sequence, including the transient, begins when the shear suppression mechanism is still strong, indicating that the transitions in this scenario are not due to spontaneous collapse of the transport barrier but instead are triggered by some instability. This is true in "hard" (with the transient) and "soft" (no large transient) transitions. Second, while searching for clues about instabilities before the transition, we find the so-called "Modulating Pedestal Mode" (MPM) and characterize its properties in Section IV. The MPM appears ~100 ms prior to the transition sequences in these experiments and grows in amplitude until the transition begins. It is significant as the large transients in D_α at the start of hard H-L sequences and the small type-III ELMs at the start of soft H-L sequences are synchronous with modulations of the MPM in all cases observed. Third, in Section V, we examine potential control strategies for mitigating or eliminating the transient and find that shots with low toroidal rotation in the co-current direction are associated with "soft" H-L transitions, which do not begin with sudden relaxations of the pedestal. "Hard" H-L transitions, which are initiated by the transient, occur when toroidal rotation is faster in the co-current direction. Rotation is controlled by adjusting the balance of power input by co- and counter-injecting neutral beams.

II. EXPERIMENT SETUP

These DIII-D[17,18] shots were performed using the parameters listed in Table I. The evolution of a typical H-mode is shown in Fig. 1: A forward L-H transition completes at 3540 ms, and the plasma is in ELM-free H-mode until the type-I ELMs begin at 3770 ms. The primary heating phase lasts until 4200 ms, after which neutral beam injection (NBI) is only used for diagnostic purposes. The last type-I ELM occurs at 4230 ms. During the following ELM-free period, pedestal density accumulates while the pedestal electron temperature decays, resulting in a pedestal pressure that remains fairly steady. At 4402 ms, a rapid (~1 ms) event similar to the type-I ELMs reduces the pedestal density by ≈50%, relaxes the pedestal pressure gradient, and releases

TABLE I. Typical shot parameters.

Symbol	Value	Name
B_t	−2.15 T	Toroidal field
I_p	1.0 MA	Plasma current
β_N	1.0–2.0	Normalized beta
q_{95}	4.6–4.9	Safety factor at 95% flux surf.
κ	1.75	Elongation
δ	0.3	Triangularity
a	0.58 m	Minor radius
R_m	1.74–1.77 m	R: Major radius
R_{xpt}	1.53 m	R, dominant X-point
Z_{xpt}	−1.17 m	Z, dominant X-point
P_{inj}	3300 kW (heat) 160 kW (diag.)	Average neutral beam power injected
$\bar{n}_e$	$1.7 \times 10^{19}/\mathrm{m}^3$	Line average density before L-H transition

~10% of the total plasma stored energy, which is typically 300 − 400 kJ before the reduction in these cases. The rest of the dithering transition sequence follows. In some shots, a de-rated neutral beam (reduced accelerating voltage and perveance to produce lower power) was running continuously during the H-mode termination phase (which would be about 4200 − 4500 ms in the example of Fig. 1: the blue shaded area with some margin) to allow measurements with Beam Emission Spectroscopy (BES),[19] while modulated beams for Charge Exchange Recombination spectroscopy (CER)[20] were used alone in others (as in the example of Fig. 1).

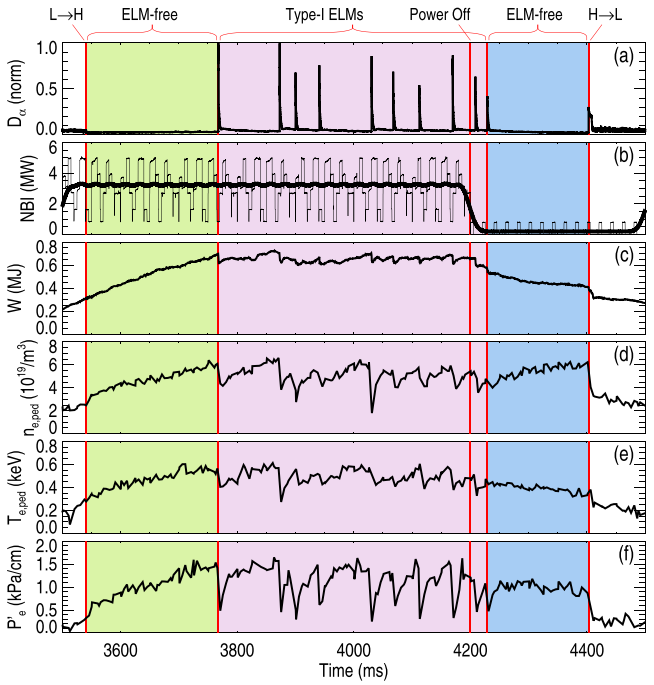

FIG. 1. History of H-mode from the conclusion of the L-H transition sequence until the beginning of the H-L sequence. (a) D_α emission from the outer strike point and (b) neutral beam injected power. The modulations are for diagnostic reasons and the average is shown by the thick line, (c) plasma stored energy, (d) electron density pedestal height, (e) electron temperature pedestal height, (f) pedestal electron pressure gradient. Electron quantities determined from tanh fits[21] to Thomson scattering data.[22] Shot 154749.

III. EVOLUTION OF E × B SHEAR PRIOR TO H-L SEQUENCE

A. E×B shear layer collapse hypothesis

Turbulence suppression by radially sheared $E \times B$ flows has been identified as the mechanism for sustaining the H-mode transport barrier.[3,23–28] The sheared $E \times B$ flow is hypothesized to reduce the radial extent of turbulent eddies, which reduces radial transport and allows a steepened pressure gradient to form.[27] In another interpretation,[29,30] energy is transferred from turbulence into benign fluctuations that do not cause radial transport. Both pictures agree that radial flow shear leads to turbulence suppression. Logically, a reduction in flow shear could weaken the transport barrier. Should the shearing rate ($\omega_{E\times B} \sim \partial v_{E\times B}/\partial r$) decay to the point that turbulent transport began to recover, then the gradients in the pedestal would be reduced. Reduction in the diamagnetic contribution to the radial electric field from the pedestal pressure gradient would further weaken the shear suppression mechanism, allowing turbulent transport to increase. If this process fed back on itself quickly enough, the edge pressure could be very quickly reduced to L-mode levels, and the resulting outflow of material would cause a flash of D_α light at the strike point, consistent with the observed transient at the beginning of the H-L transition sequence, which is shown, along with the experimental setup, in Section II. The critical test is whether the shearing rate ($\omega_{E\times B}$) decays before the transition sequence begins and becomes comparable to the turbulence decorrelation rate (ω_T) when the transient occurs. It will be shown in Section III that decay of $\omega_{E\times B}$ is quite small and that the transient occurs when $\omega_{E\times B} > \omega_T$, so the transient is not triggered by a rapid increase in turbulence resulting from the collapse of the shear suppression mechanism. This motivates the search for a different explanation, leading to the investigation of the MPM in Section IV.

B. Measurement of E × B shear prior to H-L sequence

Measurements of $\omega_{E\times B}$ were made using CER. The radial electric field was calculated from force balance using Eq. (1), which is valid if pressure p, density n, and flow velocity v are measured for the same species (fully stripped carbon in this case: charge state $Z = +6$).[27]

$$E_r = \frac{\partial p/\partial r}{Zen} - v_\theta B_\phi + v_\phi B_\theta. \quad (1)$$

The shearing rate for flute like turbulence ($\Delta\eta \gg 1$, in contrast to ballooning-like turbulence: $\Delta\eta \sim \pi$, where $\mathcal{J}B\Delta\eta$ is the parallel correlation length[25] and $\mathcal{J} = (\vec{\nabla}\psi \times \vec{\nabla}\phi \cdot \vec{\nabla}\theta)^{-1}$ is the Jacobian) as a result of shear in the $v_{E\times B}$ drift[27] is given by the following equation:

$$\omega_{E\times B} = \frac{(RB_\theta)^2}{B}\frac{\partial}{\partial\psi}\omega_E. \quad (2)$$

The $E \times B$ rotation frequency $\omega_E = E_r/RB_\theta$ is calculated from CER measurements and then fit to Eq. (A1), [31] which may be found in the Appendix. For comparison, the plasma frame turbulence decorrelation rate ω_T is computed using data from vertically separated BES chords as described in Subsection 2 of Appendix A.

The results are shown in Figs. 2 and 3 for typical back transitions with and without the initial transient, respectively (means of avoiding the transient are documented in Section V). Reduction in turbulent transport by $E \times B$ flow shear should be expected when $\omega_{E\times B} \gg \omega_T$ (H-mode), with $\omega_{E\times B} \approx \omega_T$ resulting in a weaker suppression effect (not H-mode).[25] These results show that $\omega_{E\times B}$ remains well above ω_T until after the back transition sequence begins in both cases. Furthermore, the ratio $\omega_{E\times B}/\omega_T$ is fairly steady at values well above 1. In order for a back transition to be initiated by spontaneous failure of the shear layer, $\omega_{E\times B}/\omega_T$ would have to decay leading up to the transition. Thus, the back transition sequence is not triggered by decay of $\omega_{E\times B}$ during the period before the start of the sequence and some other mechanism must be responsible.

IV. CHARACTERIZATION OF MODULATING PEDESTAL MODE

Since the hard H-L back transition transient is not an ideal P-B type-I ELM[1] and is not due to spontaneous collapse of $E \times B$ shear suppression, we now seek to understand the start of the H-L sequence by examining the properties of fluctuations in the pedestal prior to the start of the sequence.

During the ELM-free period starting shortly after NBI power is reduced to minimal diagnostic levels and before the

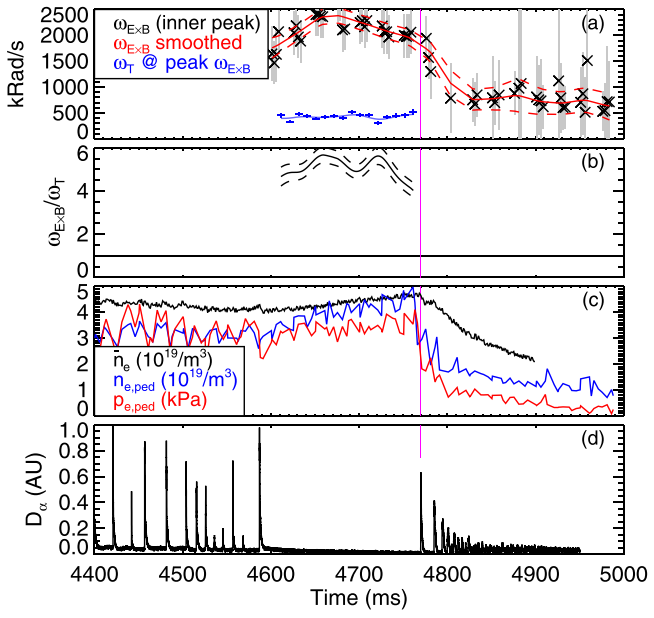

FIG. 2. $\omega_{E\times B}$ and ω_T comparison for the termination phase of an H-mode with a hard H-L transition. (a) Value of $\omega_{E\times B}$ at the peak at the inside of the E_r well (data: black X w/ gray error bar; smoothed trend: solid red line with propagated uncertainty indicated by dashed red lines); ω_T (blue) calculated during the ELM-free period prior to the beginning of the transition sequence. (b) $\omega_{E\times B}/\omega_T$. (c) Line average density (black), pedestal e^- density (blue), and pedestal e^- pressure (red). (d) D_α emission at the outer strike point. NBI was reduced to diagnostic levels at 4505 ms. Most quantities from shot 159355, with beams setup for best CER data quality. Decorrelation rate calculated from matched shot 154754, which used beams for BES. The time sequences are aligned at the transient.

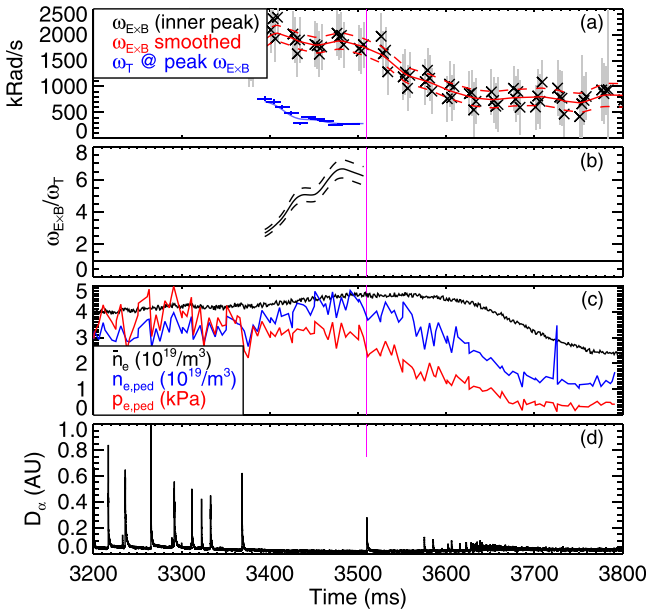

FIG. 3. $\omega_{E\times B}$ and ω_T comparison for the termination phase of an H-mode with a soft H-L transition. Compare with Fig. 2. NBI was reduced to diagnostic levels at 3300 ms. Most quantities from shot 159354. Decorrelation rate calculated from matched shot 159358.

start of back transition activity, a powerful coherent fluctuation is seen with consistent properties in all fast density measurements: BES, Doppler Back Scattering (DBS),[32] Millimeter-wave Imaging Reflectometer (MIR),[33] and the CO_2 interferometer.[34] Unfortunately, fast electron temperature measurements from the Electron Cyclotron Emission (ECE)[35] diagnostic are unavailable because typical densities in these experiments result in cut-off of the critical ECE chords. DIII-D's magnetic probe system[36] is also challenged as the poloidal wavelength of the MPM is roughly equal to the length of the pickup coils that are used for measuring changes in the magnetic field. The MPM is observed before the start of both hard and soft H-L transition sequences and also commonly reappears between the first few dithers or type-III ELMs of the sequence.

The layout of BES chords is shown in Fig. 4. Data from BES column 6 will be used unless otherwise specified.

The following sub sections will detail the signature of the MPM on spectrograms of rapid density fluctuations (Sec. IV A), examine modulations in amplitude and propagation velocity of the MPM (Sec. IV B), analyze the dispersion properties of the MPM (Sec. IV C), and determine the radial and poloidal localization of the peak fluctuation power associated with the MPM (Sec. IV D).

A. Fluctuation spectra evolution prior to the H-L back transition

Spectrograms of density fluctuations measured with BES during the termination phases of example H-modes with hard and soft back transitions are shown in Fig. 5. In the hard (soft) case, heating power was cut at 2150 ms (4400 ms), type-I ELMs stopped at 2210 ms (4424 ms), and the beam used for BES measurements was turned on at 2260 ms (4400 ms). It can be seen that, for both cases, the

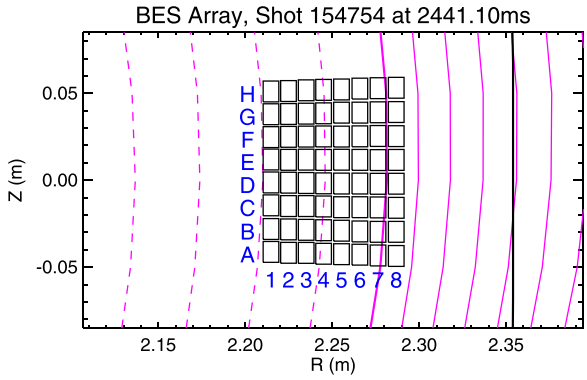

FIG. 4. Spatial position of BES chords relative to representative separatrix (thick magenta line between columns 7 and 8), flux surfaces (dashed: closed, solid: open), and limiting surface (black line).

fluctuation power peaks between 40 and 80 kHz and grows in amplitude until the event at 2442 ms (4653 ms), which is associated with a bright burst of D_α emission from the divertor strike point in the case of the hard H-L transition sequence. For this type of event, which is discussed in more detail later, the associated D_α spike can be large, small (like the type-III ELMs), or absent [as in the example shown in Fig. 5(d)] and the size or absence of the D_α spike is qualitatively consistent across all filterscope chords in the upper and lower divertors and those tangent to the edge of the plasma at the outboard midplane. It can be seen that the mode has some spectral sidebands. The bands are roughly 5 kHz apart at 2400 ms (4630 ms), but they can be seen to contract together over time.

Despite dramatic differences in the outcome of the first "event" of the sequence (which is a rapid slowdown of the MPM's propagation velocity, as shown in Section IV B), there is no obvious difference in the MPM between cases with hard and soft H-L transitions. Thus, the following characterization of the MPM applies to both hard and soft cases.

Several magnetic probes do pick up pieces of MPM's spectral signature, consistent with the measurements shown in Fig. 5. The signature appears more strongly on a subset of probes that have smaller physical dimensions than is typical (they have $\approx 1/3$ of typical length), although all but one of these also include significant noise. Figure 6(a) shows the spectrum of magnetic fluctuation power on a linear color scale for the single short probe without high noise. The noise problem is demonstrated in Fig. 6(b), which is the spectrum of another short probe but with obvious pollution at about 55 and 70 kHz, preventing analysis of the critical part of the spectrum. Figure 6(c) shows the result from one of the longer probes with vertical length comparable to the vertical wavelength of MPM. It can be seen that the signal is very weak compared to the background, but there is a hint of MPM activity at around 70 kHz and 2425 ms. From these measurements, we can conclude only that the MPM is not electrostatic as its signature has been picked up by the one probe which has appropriate dimensions and low noise. The poor ability of all of the other probes to diagnose the MPM prevents many standard magnetic analysis techniques, including confident determination of toroidal mode number.

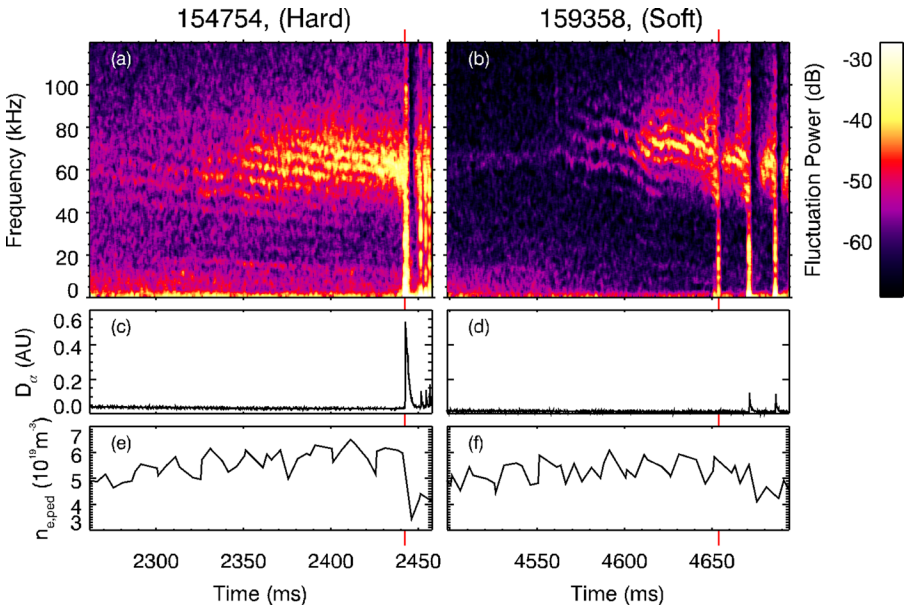

FIG. 5. Spectrograms of a BES chord aimed at the steep gradient region, measuring fast density fluctuations before the start of a hard H-L transition sequence (a) and a soft transition (b). The fluctuation properties are very similar, despite obvious differences in the corresponding time histories of D_α emissions from the outer strike point (c and d) and pedestal density (e and f). The FFT windows are 4096 samples (4.096 ms) each with 95% overlap. The D_α traces are normalized to the large type-I ELMs which occurred earlier in the shot, before the start of the display time window. In the case of the hard transition, the large transient at 2442.37 ms, easily identified by the D_α spike in (c) is associated with a vertical stripe in the spectrogram (a). Similar fluctuation behavior before the soft transition [at 4653.76 ms, see (b)] does not always result in any spike in D_α emission, such as in this example.

B. Amplitude and propagation velocity modulations of the MPM prior to the H-L transition

The mode amplitude is modulated at ≈2 kHz before the transition sequence begins, as seen in Fig. 7. The modulation frequency is initially higher but decreases over time. This can be seen in the spacing of the sidebands in Fig. 5.

Poloidal propagation of this mode can be seen in the delay between signals on vertically separated chords with the same radial position; the MPM propagates in the electron diamagnetic direction, which is also the direction of $v_{E\times B}$ in the E_r well. The BES diagnostic produces two types of measurements: there is a fast signal that is AC coupled and digitized at 1 MS/s for detecting high frequency fluctuations and a slow signal which is DC coupled and digitized at 10 kS/s. The ratio of fast/slow BES intensity $\tilde{I}/I$ is proportional to $\tilde{n}/n$.[19] Figure 8 shows contours of $\tilde{I}/I \propto \tilde{n}/n$. The tilt of these contours is due to the poloidal propagation velocity v_p, with faster moving features producing more vertically oriented stripes and slowly propagating features producing more horizontally oriented stripes. It can be seen that as the mode amplitude grows (stripes become "brighter"), the propagation velocity slows down (the stripes tilt over to the right more). By 2442.37 ms (0 on the plot axis), the perturbation slows and eventually stops at the time when the hard back transition occurs. The propagation velocity prior to the slowdown is consistent with the local $E \times B$ drift velocity within the uncertainty in the relative positions[37,38] of CER and BES chords. The slowdown happens in ∼100 μs, whereas CER is configured with a 2.5 ms averaging window and the beams are pulsed on for 5 − 10 ms out of every 25 ms. Therefore, it cannot be determined from these data whether $v_{E\times B}$ experiences a temporary reduction during the D_α spike or if v_p departs from $v_{E\times B}$.

The dominant frequency and wavenumber of the MPM are found using the method described in Appendix B. From these, the lab frame propagation velocity v_p and amplitude of the dominant frequency component are found as well. The results are plotted in Figure 9, along with D_α for reference. It can be seen in Fig. 9 that all of the quantities of interest are experiencing modulation. The modulations in dominant frequency and wavenumber are phased to produce minimal change in v_p for most of the time window, but changes in

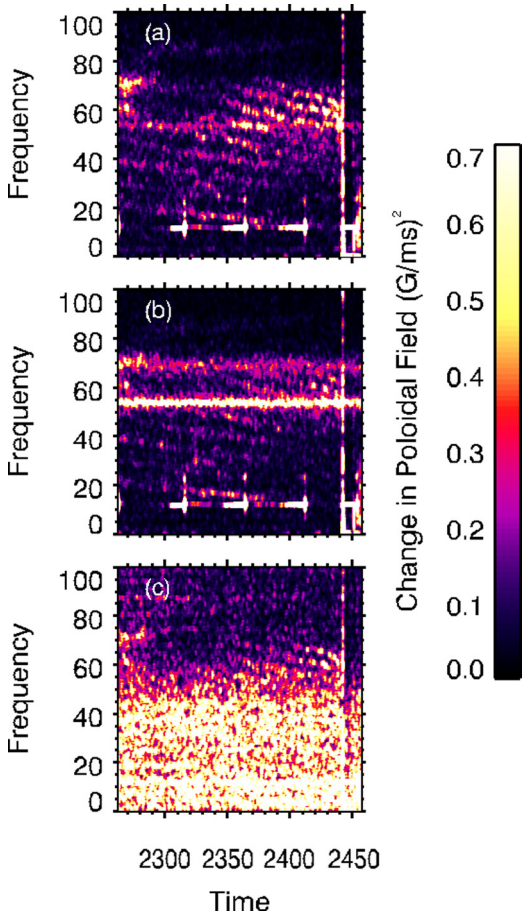

FIG. 6. Magnetic fluctuation spectra for three $\dot{B}_\theta$ probes at the machine midplane. (a) A short ($L_\theta = 5.5$ cm) probe with low noise which detects the MPM's signature. (b) Another short probe which experiences high noise in the relevant frequency range. (c) A long ($L_\theta = 14$ cm) probe with weak pickup of the MPM ($\lambda_\theta \approx 20$ cm).

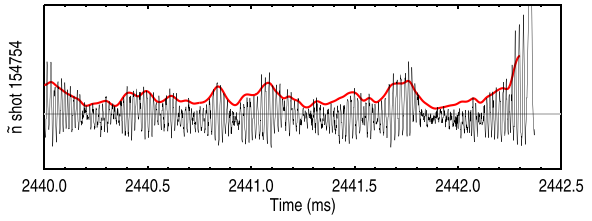

FIG. 7. 1 MS/s, AC coupled BES signal measuring short timescale density fluctuations from the same chord as was used in Fig. 5(a). The thick red line behind the raw signal is a smoothed Hilbert envelope: $A = |y + iH(y)|$, where $i = \sqrt{-1}$ and H() is the Hilbert transform. It can be seen that there is a clear fundamental frequency. Thus, the MPM is coherent and the sidebands in the spectrogram are simply the result of amplitude and frequency modulation.

propagation velocity become more significant before the event at 2442.37 ms. During the penultimate peak in amplitude, just before 2442 ms, the propagation velocity drops noticeably (marked by a blue arrow in Fig. 9(d)). There is another drop in v_p just before the D_α spike begins; this time v_p drops to ≈0 in a behavior that, for convenience, will be referred to as "locking."

From the measured $k_z \simeq -k_\theta \approx 30\ \mathrm{m}^{-1}$, the diameter of the plasma cross section at the midplane $R_{mid,out} - R_{mid,in} = 1.15$ m, the local safety factor $q = 4.7$, and the assumption that the mode is field aligned, we estimate the poloidal mode number $m = 17$ and the toroidal mode number $n = 3$ or 4. Testing for field alignment on DIII-D would require good results from the magnetic probe system, which is unfortunately not well suited to diagnose the MPM. However, it would be surprising if the MPM's structure were not extended along the field lines.

C. Evolution of the MPM dispersion relation leading up to the H-L transition

While Section IV B showed f and k for the dominant component, it is also useful to view the dispersion relation of the entire spectrum. This is accomplished by the local wavenumber analysis described in Appendix C and shown in Figure 10 for time windows during the ELM-free periods prior to the beginning of back transition sequence seen in Fig. 5(b). BES and MIR data are shown in Figure 10 for comparison. MIR measures k_θ along flux surfaces, while BES measures k_z from a vertical stack of chords, and k_z

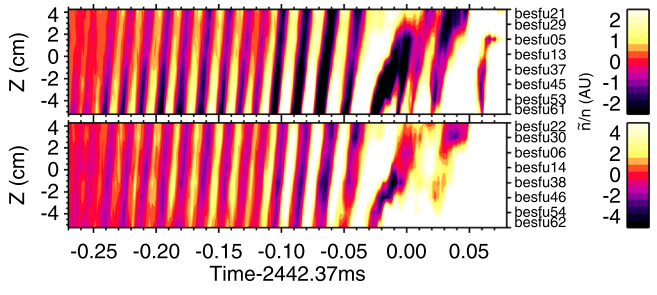

FIG. 8. Contours of BES $\tilde{I}/I \propto \tilde{n}/n$,[19] for shot 154754 with a back transition starting near the end of the time window. The two plots show BES data from columns of chords at $R = 225.5$ and 226.6 cm, respectively (columns 5 and 6, see Fig. 4). The chosen columns had the strongest indication of the MPM. The time is given relative to the large spike in D_α emission, which begins at 2442.37 ms. The lower plot includes the chord used for Fig. 5(a).

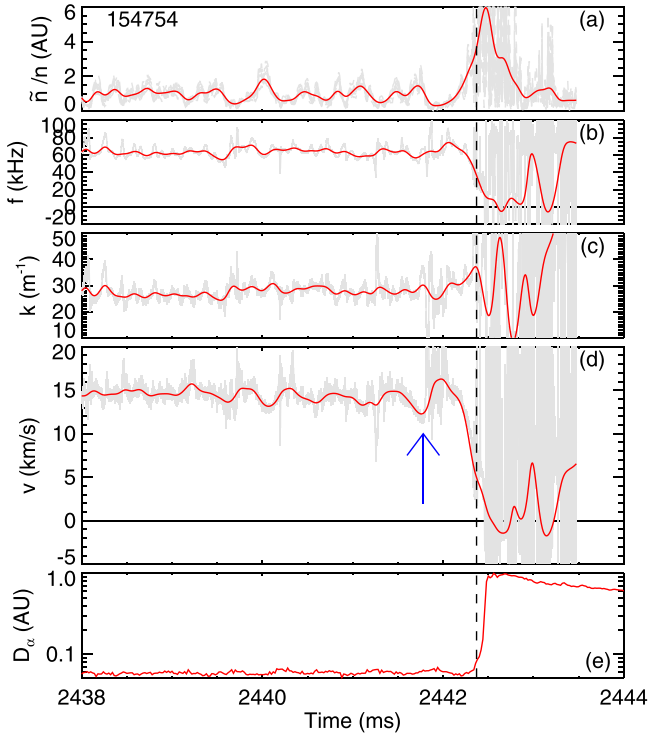

FIG. 9. Time histories of (a) amplitude ($\tilde{n}/n$), (b) frequency, (c) wavenumber, (d) propagation velocity, and (e) semi-log plot of D_α from a photodiode aimed at the outer strike point. f and k are calculated by the fit to Eq. (B1). A back transition begins at 2442.37 ms, marked by a vertical black dashed line. The smoothed results are plotted in red with the un-smoothed results in light gray to give a sense of the scatter produced by this method. Positive velocity indicates propagation vertically upward at the outboard midplane.

$\simeq -k_\theta$ near the midplane. The lower spatial resolution of MIR relative to BES results in more smearing in k, but the results are consistent. It can be seen that all of the frequency components of the MPM lie along a straight line intersecting $k = 0, f = 0$: the fundamental and the sidebands propagate at the same propagation velocity v_p. This means that the amplitude modulation is propagating with the mode. In contrast, a purely time dependent modulation would produce sidebands at constant k but different v_p.

D. Spatial localization of the MPM

The MPM radial position is strongly localized. The banded structure seen in the spectrograms of Figs. 5(a) and

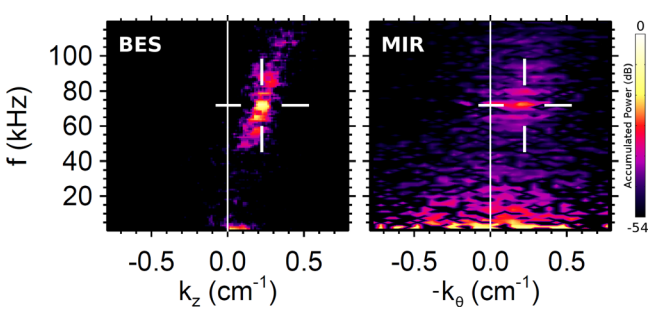

FIG. 10. Dispersion plot: power vs. k, f for 3 ms of BES data (left) and 10 ms of MIR data (right). k is calculated from the cross-phase between chord pairs (see Eq. (C1)). Data are aggregated from several chord pairs in a vertical column (BES) or along a flux surface (MIR). This data set corresponds to Fig. 5(b) at 4630 ms.

5(b) emerges very clearly from the background on chords from only three columns in the BES array (5, 6, and 7; see Fig. 4). The signature is fainter or undetectable on chords located farther out or deeper into the plasma. This is also reflected in the profile of $\tilde{n}/n$: Figure 11(a) shows the spatially and temporally resolved amplitude of fluctuations during the ELM-free period prior to the start of the back transition sequence, frequency averaged between 40 and 80 kHz. From this plot, it is clear that this mode is localized to a width of a few % in ψ_N. Figure 11(b) shows the electron pressure gradient for comparison, demonstrating that the MPM is localized to the steep gradient region.

The mode is further localized to the low field side by using a CO_2 interferometer[34] that measures line integrated density along three vertical chords at the V1, V2, and V3 ports at $R = 1.48$, 1.94, and 2.10 m (compare to $R_m = 1.75$ m and $R_m + a = 2.28$ m) and one horizontal chord at the R0 port (midplane). Although the chords sample primarily through the core, the mode being studied is strong enough that it still stands out against the background of other fluctuations picked up along the length of the interferometer chord. That is, density fluctuations with the same temporal and frequency evolution as shown in the BES data [Figs. 5(a) and 5(b)], including the spectral sidebands, are present in spectrograms from the interferometer. The characteristic banded structure is seen clearly in the spectrogram (not shown) of the vertical chord V3 at large R on the low-field side and is almost undetectable by chord V1 on the high-field side.

Figure 12 shows the distribution of power in the relevant frequency band on different interferometer chords. The average measured fluctuation power normalized to the length of the interferometer chords in the region $0.92 < \psi_N < 0.97$ reveals that these fluctuations have at least $\approx 10\times$ more power on the low-field side V3 chord than on the V1 chord that samples the high-field side. A significant increase in power is seen from V2 to V3, which are 16 cm apart and both on the low-field side. If one assumes that the power picked up by the R0 chord is strongly dominated by the low field side contribution, then all of this power can be assigned to a radial position ≈ 15 cm outboard of V3 and the intersection length can be halved, giving a normalized power greater than double that of V3 and indicating even stronger localization. Of course, not all power in the chosen frequency band has to come from the mode, so this technique underestimates the degree of localization. Thus it is concluded that the MPM is radially localized slightly inside the separatrix and to the low-field side. It is consistent with an instability of ballooning character.

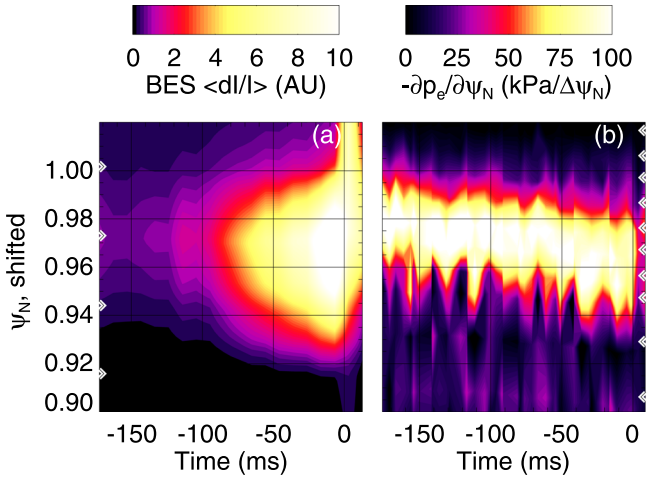

FIG. 11. Comparison of spatial localization of density fluctuations with $40 \leq f \leq 80$ kHz measured by BES to ∇p_e measured by Thomson scattering (TS). Primary heating power is cut at 2150 ms and a hard back transition sequence begins at 2442 ms. (a) BES intensity fluctuation power normalized to average intensity (ratio of fast to slow signals, proportional to $\tilde{n}/n$). All 64 BES chords in a square array (see Fig. 4) at the outboard midplane are mapped to ψ_N. FFT windows are 10 ms long and power is averaged over the selected frequency band. (b) $-\partial p_e/\partial \psi_N$. An EFIT[39] equilibrium reconstruction with shifts to correct the alignment of the profiles (see Appendix D) is used for mapping to ψ_N. Triangles at the edges of the plots indicate the spatial resolution of (a) BES and (b) TS. The limited resolution of the BES compared to TS explains why movement of the peak ∇p in (b) is not reflected by BES measurements in (a).

While ideal, linear ballooning instability was eliminated as a trigger for the H-L transient by previous work,[1] a resistive, kinetic, or nonlinear variant could still be unstable before the H-L transition and might explain the MPM or the transient. As seen in Figure 1, temperature decreases after the beams are turned off, so resistivity ($\eta \sim T_e^{-1.5}$) increases. Decreases in temperature are balanced by increases in density to maintain a nearly steady pressure gradient. Resistive ballooning mode drive is roughly proportional to $\eta \nabla p$ and should be increasing.[40] The lifetime of the MPM (>100 ms) is far longer than linear growth timescales for common ideal or resistive instabilities. For comparison, typical linear growth timescales for ideal instabilities are on the order of the Alfvén time $\tau_A \sim 1\ \mu$s,[10,41–43] whereas the linear growth of resistive wall modes (which are among the slowest growing linear instabilities) is determined largely by the timescale for flux to diffuse through the wall of the vacuum vessel $\tau_w \sim 1 - 10$ ms in DIII-D.[43–45] However, nonlinear instabilities such as tearing modes[46,47] can evolve on longer timescales of $\gtrsim 100$ ms.[48] This suggests that the nonlinear dynamics of the mode are important. If, for example, the mode were nonlinearly saturated, then amplitude would increase with drive. If the drive were proportional to resistivity, then the mode amplitude should slowly evolve during the ELM free period before the back transition, consistent with the observations shown in Figure 13.

V. CONDITIONS FOR SOFT H-L TRANSITIONS

Soft H-L transitions (without the large transients at the start of the sequences) were observed in four cases: after very short H-modes, after H-modes powered by ECH, in connection with a sudden shape change executed in anticipation of the transient, and after H-modes that received primary heating from NBI counter to the plasma current.

The short H-modes terminate before triggering any type-I ELMs and have durations of ≈ 100 ms or less, which is comparable to or shorter than the length of the termination phases of the H-modes studied in earlier sections (see Fig. 5). These cases probably do not have enough time to evolve to a state that can drive the hard back transition. Regardless of the reason for the soft transitions out of short

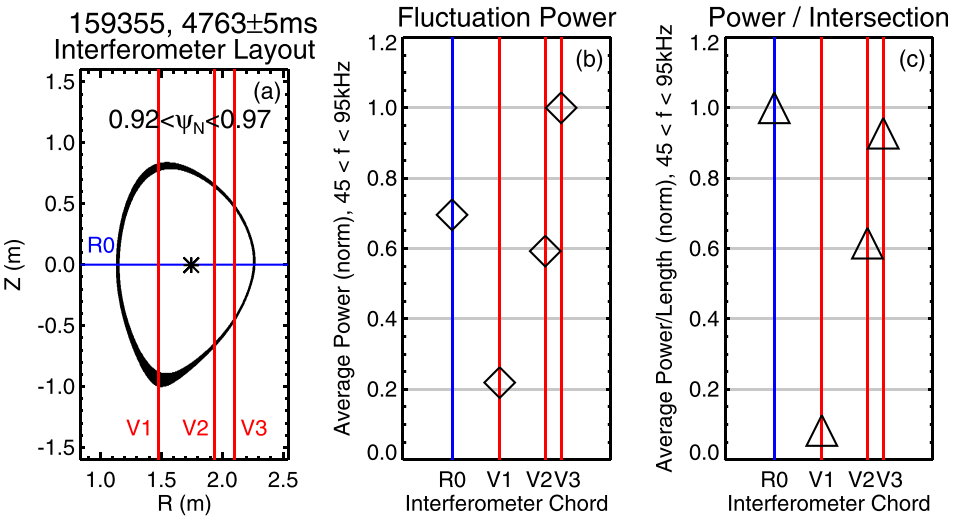

FIG. 12. Localization to the low field side by the interferometer. (a) Physical positions of the interferometer chords (blue and red lines) compared to the pedestal region of the plasma (black). A black asterisk marks the magnetic axis. (b) Average fluctuation power for $45 < f < 95$ kHz. (c) Fluctuation power from (b) divided by the lengths of the intersections of the chords with the pedestal region. The start of back transition activity starts shortly (<1 ms) after the end of the time window from which data were taken. The horizontal spacing between the points for the vertical chords in (b) and (c) is proportional to the physical locations of the chords; R0 has been placed arbitrarily for ease of viewing.

H-modes, they are of little interest. Strategies for producing soft H-L transitions should be distinguished from the short H-mode case by comparison between H-modes of similar length with soft and hard H-L transitions or by the presence of type-I ELMs at some point in the H-mode. Empirically, co-NBI heated plasmas with our setup always experience hard back transitions after ELMing. So, presumably an ELMing plasma has had enough time to evolve to the point where hard back transitions can be triggered.

The ECH H-modes were compared to NBI H-modes of similar length. The H-L sequences following ECH were soft, whereas the post-NBI cases were hard, as seen in Fig. 14. So, use of ECH instead of NBI heating tends to help produce a soft H-L transition sequence. Although several examples similar to Fig. 14 exist, none of the ECH phases from this experiment lasted long enough to produce ELMs. It is not clear whether substituting ECH for NBI would allow a soft transition out of a type-I ELMing plasma in this scenario and more testing would be needed to determine this.

The sudden shape change involved an increase in upper triangularity designed to modify the coupling strength between peeling and ballooning modes and move the P-B boundary in $p' - J$ space. This scheme was conceived of before the transient was shown to be stable to ideal P-B modes.[1] The critical pressure gradient for a strongly coupled P-B mode is a strong function of upper triangularity[6,10] and thus a rapid enough shape change should be able to temporarily outrun increases in pressure gradient, providing an opportunity for some other process to take over and initiate the H-L sequence. Since the common initiator is not a strongly coupled ideal P-B mode[1] and p' is not increasing before the transition starts, this technique should not work as expected. Despite these arguments, the technique appears to be successful in removing the transient. Figure 15 shows the results of a sudden triangularity increase in anticipation of the H-L transition, where the H-L sequence on the right side of the figure is initiated by a much smaller D_α spike than the sequence on the left side of the figure, and stored energy

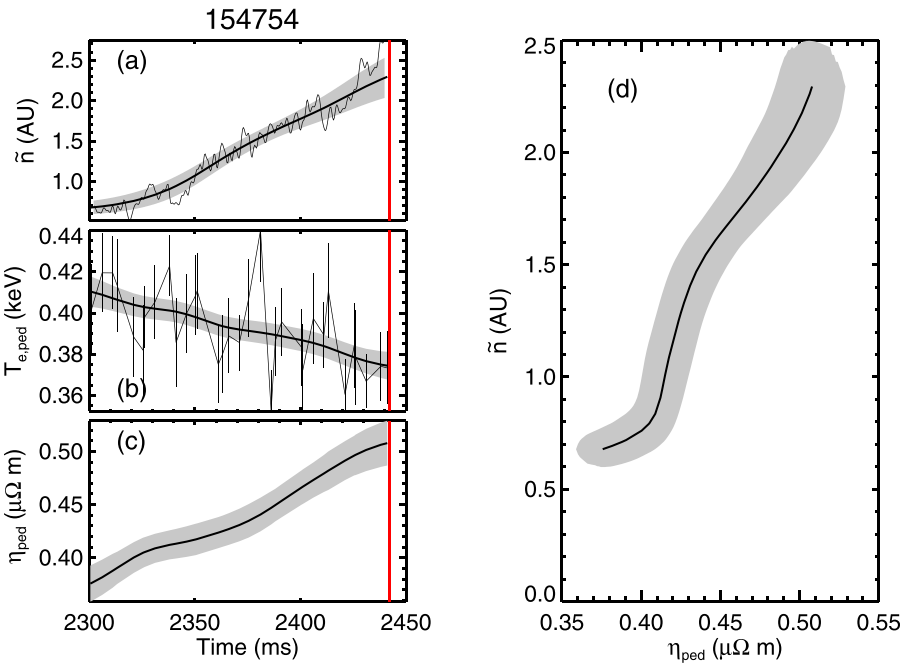

FIG. 13. Relationship of MPM amplitude with resistivity. Time histories of (a) MPM amplitude, (b) electron temperature at the top of the pedestal, (c) Spitzer transverse resistivity at the top of the pedestal,[49] and (d) amplitude vs. resistivity. The gray area represents uncertainty determined by (a) local standard deviation (essentially a measure of high frequency changes that are treated as noise), (b) experimental uncertainties propagated through the smoothing kernel, and (c) standard deviation of 200 Monte-Carlo trials using experimental uncertainty in n_e, T_e, and assuming 10% error in the effective ion charge state Z_{eff}.

decreases smoothly, rather than falling suddenly in one step. When the triangularity excursion was not timed correctly or was absent, the transient occurred. It is clear that the quick change is important: in the example shown in Fig. 15, triangularity increases from 0.2 to 0.4. Simply running the discharge at triangularity of 0.4 does not prevent the transient from occurring; instead, triangularity must be set to a lower value and then be increased quickly at the correct time. The transient resulted if the shape change occurred too soon such that the sequence began late in the flat top of the triangularity excursion. It would be useful to conduct further testing to determine whether this technique would work in the termination phase of an H-mode that had been heated for long enough to produce type-I ELMs.

The most robust method for producing soft H-L transition sequences is through application of counter-torque during the primary heating phase. Figure 16 shows an example of this behavior. In particular, Fig. 16(a) compared to Fig. 16(b), 16(c) shows a large difference in the brightness of the initial D_α flash, and the plots of pedestal density (g) and stored energy (j) show sharp drops associated with the transient at the start of the hard back transition in contrast to the soft transitions, where density (h,i) and energy (k,l) decrease more smoothly. It can be seen from the figure that although the rotation imparted by the beams decays after primary heating power is removed, a significant difference remains at the start of the H-L transition sequence [Figs. 16(d)–16(f)]. The start of the sequence is being defined by the locking behavior of the MPM (see Section IV) and marked by dotted vertical lines. The beams used for diagnostics introduce a small amount of co-torque during the termination phase: blips for CER add an average of +0.2 to +0.3 Nm co-torque and continuous beam usage for BES adds about +1.0 Nm. For comparison, torque injected during the heating phase is −3.3 to −2.6 Nm or +2.7 Nm to +3.9 Nm for counter and co setups.

Many counter-torque H-modes were produced and they reliably underwent soft back transitions. The counter-torque shots were interleaved with co-torque shots, which continued to produce hard back transitions. A pair of co-torque shots with hard transitions was surrounded by counter and balanced torque shots, which experienced soft transitions, and the counter torque shots were surrounded by co-torque shots with hard transitions. So, the difference does not appear to result from wall loading or other evolving conditions inside the vacuum vessel. Because of the interleaving of co and counter torque shots, it was easy to find hard counterparts for soft transitions. It was found that for most co/counter pairs of transitions, the only significant difference in the basic measurements was in the toroidal rotation. Electron temperature and density profiles were essentially identical in most cases, as was the depth of the E_r well.

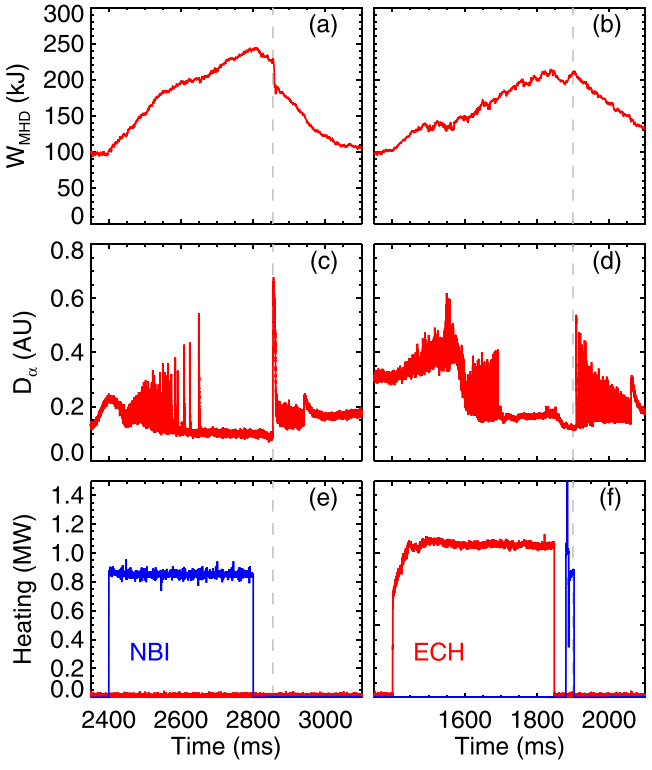

FIG. 14. Comparison of H-L sequences following short NBI and ECH powered H-modes. A vertical dashed gray line indicates the start of the H-L sequence. (a) Shows a step down in stored energy associated with a single prominent D_α flash (c), which stands out from its neighbors when the plasma is heated with NBI (e). (b) shows more gradual release of energy with no discontinuity and no stand-out D_α flash (d) when heating power comes from ECH (f). There is a pulse of NBI in (f) to enable some beam dependent diagnostics, but the momentum imparted by such a short pulse is small.

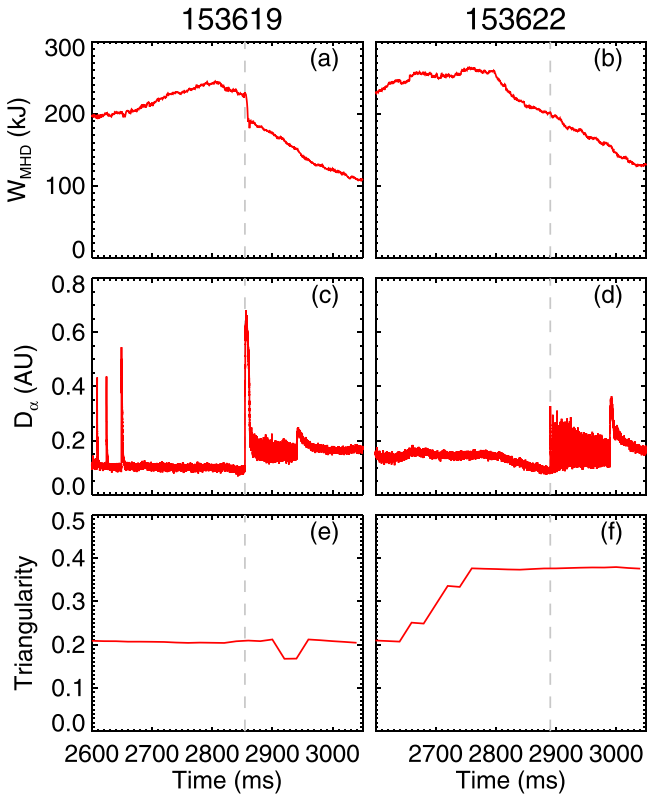

FIG. 15. H-L transition sequences with and without a sudden change in the plasma boundary shape prior to the transition. A dashed vertical gray line marks the start of the H-L sequence. (a) Stored energy, showing a sudden drop associated with the large D_α flash in (c) in a case with no intervention, as seen by the steady value of the triangularity shaping parameter in (e). (b) Stored energy with no sudden drops and no large D_α flash (d) in a case where the triangularity shaping parameter (f) was rapidly increased in anticipation of the H-L sequence.

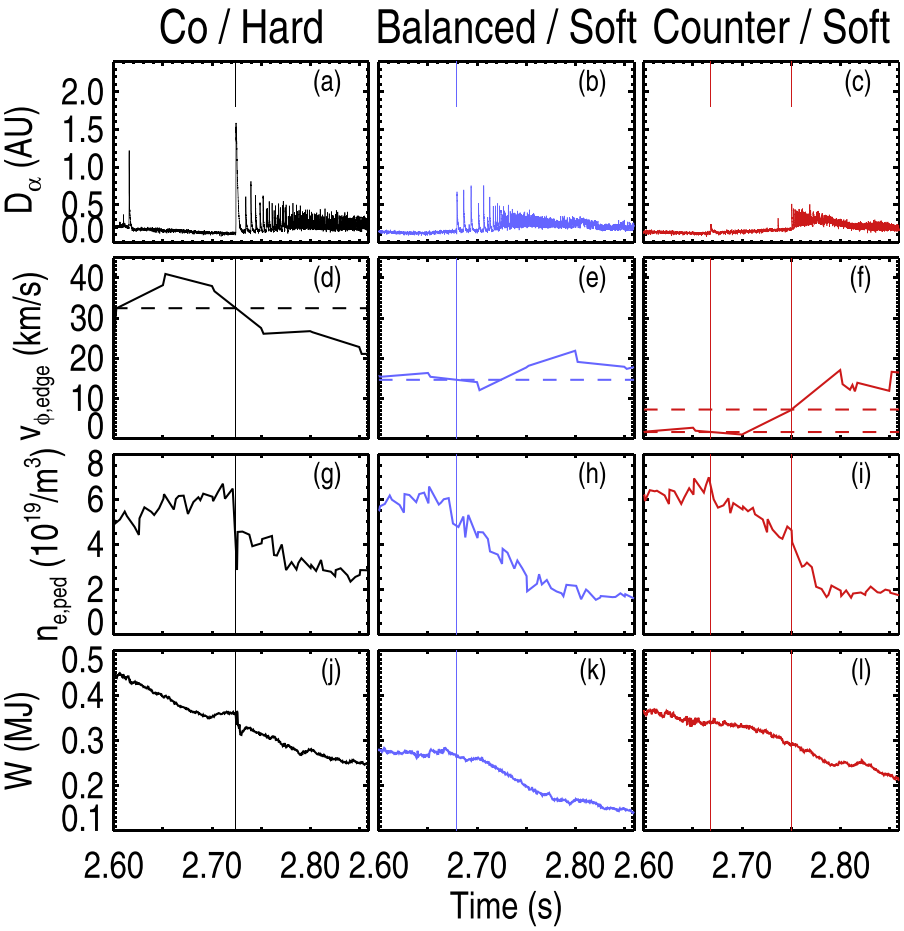

FIG. 16. Control of the transient associated with H-L transition sequences by varying NBI torque. Power during the primary heating phase was delivered by co, balanced, or counter injecting beams, which were then turned off to allow a back transition. (a) Large D_α flash at the start of a hard H-L sequence and (b and c) smaller flashes at the start of soft H-L sequences. (d-f) Edge toroidal rotation, with the value at the start of the H-L sequence marked by a dashed horizontal line. (g-i) Pedestal density, showing a sudden step down associated with co-torque only. (j-l) Stored energy, also showing a step down for the co-torque case in contrast to gradual decreases in the balanced and counter torque cases.

Prompt energy and density losses and D_α flash brightness across the first event of the H-L sequence are plotted vs. edge toroidal rotation frequency in Figure 17. It can be seen in the figure that the balanced torque cases have properties that are intermediate between the co and counter torque cases. This suggests that the large transients and small type-III ELMs at the start of hard and soft H-L transition sequences have related triggering mechanisms: the large transients may be the high rotation limit of the type-III ELMs.

VI. DISCUSSION

We find that dithering H-L transition sequences in DIII-D commonly begin when $E \times B$ shear should be strongly suppressing turbulence, indicating that the low-power ELM-free H-mode preceding the transition sequence in our scenario is promoting the growth of some instability, which reduces the pedestal height and thus weakens the diamagnetic contribution to E_r, ultimately collapsing the shear layer and terminating H-mode. This is true in "hard" back transitions, where a large transient quickly relaxes most of the pedestal pressure gradient in ~1 ms and in "soft" back transitions where the pedestal is gradually relaxed over ~100 ms by a series of type-III ELMs. In both cases, we find a coherent density fluctuation that appears in the pedestal and grows in amplitude until the start of the back transition. This MPM is implicated as a conspirator in the death of the transport barrier by the synchronization of its propagation velocity "locking" events with the transients and type-III ELMs of both types of H-L sequence. The MPM is ballooning-like in its spatial localization, its long ($\gtrsim$ 100 ms) lifetime is consistent with nonlinear saturation, and the evolution of its average amplitude tracks increasing

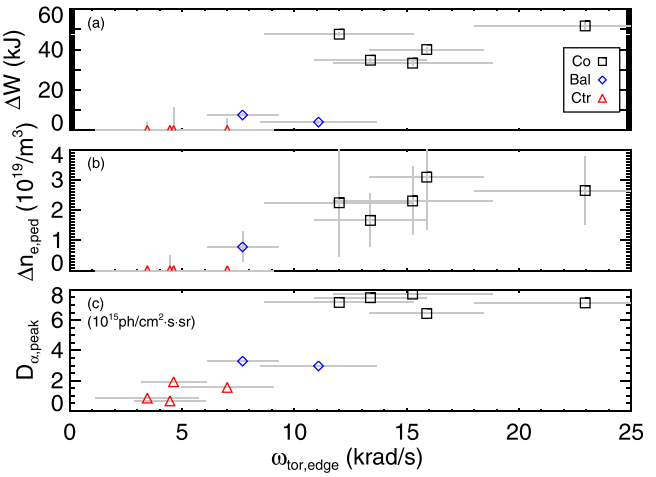

FIG. 17. Prompt energy (a) and pedestal density (b) losses and D_α flash brightness (c) vs. edge toroidal rotation frequency for the first v_p locking event. Symbols indicate the direction of neutral beam torque injection: black squares for co-torque, blue diamonds for balanced torque, and red triangles for counter-torque. Differences other than rotation and torque were minimized by selecting a set of sequential shots with identical setup and electron profiles. The prompt energy and density losses for the counter torque cases are lost in the noise. Prompt losses for balanced torque cases are small compared to co-torque cases, but they are now measurable above the noise.

resistivity in the steep pressure gradient region. These observations are consistent with a linearly unstable, nonlinearly saturated, resistive ballooning mode. Future work could test this hypothesis using a two-fluid model in a code such as BOUT++[50] while also exploring other explanations.

It was found that the expression of hard vs. soft transitions was sensitive to toroidal rotation. However, there appears to be a continuum of sizes available for the first event of the H-L sequence, as demonstrated in Figure 17. This continuum of transient/type-III ELM sizes, together with the observation of identical MPM v_p locking behavior synchronized with transients and type-III ELMs, suggests that these events are triggered the same way: the transient is a giant type-III ELM. While type-III ELMs are somewhat ill-defined,[51] it is generally agreed that they occur below the ideal ballooning limit and are probably triggered by a resistive instability.

Also of note is that although quickly co-rotating plasmas experience large transients at the start of their H-L sequences, the second v_p locking event typically results in a small type-III ELM. The reduction in toroidal rotation during the transient is not large enough to explain this. So, there must be (unsurprisingly) other parameters of importance; probably pressure gradient, but density may also be important. Variation in pre-HL electron profiles between cases was small, which helps to isolate the importance of v_{tor}.

The MPM often lasts for >100 ms and should be fairly easy to detect in real time by a growing difference in fluctuation power in interferometer measurements by two vertical chords in the relevant frequency range. This is enough time for a control system to act to suppress the transient and ensure a soft H-L transition or to increase power to avoid the transition, assuming more power is available. Applying the counter-injecting beams can reduce v_{tor} sufficiently in ~100 ms and the triangularity change takes ~100 ms, which should be fast enough to soften a back transition. The confinement time is a few hundred ms and so increased power should start to reach the edge in time to prevent an undesired back transition. This could be useful, for example, in an experiment studying H-mode close to the power threshold.

VII. CONCLUSION

The large initial transient observed in most H-L back transition sequences in our experiments is probably driven by the same mechanism as the small type-III ELMs, as both are synchronous with identical v_p locking behavior of the MPM and a continuum of transient/type-III ELM sizes appears to exist. The amplitude is very sensitive to edge toroidal rotation, which in turn may be controlled by adjusting torque inputs to the plasma. Activity associated with the dithering H-L transition sequence begins when $\omega_{E\times B} > \omega_T$ in the experiments examined, showing that the early oscillatory behavior takes place when the shear suppression mechanism is still strong. Therefore, the large transients and first type-III ELMs of soft transition sequences probably are not directly related to L-H/H-L transition physics, but rather, are responsible for relaxing the pedestal, which reduces the diamagnetic contribution to $v_{E\times B}$ and weakens the shear suppression mechanism, leading to the H-L transition proper. The modulating pedestal mode is a potential indicator of an impending H-L transition in a low powered H-mode, at least for this class of plasma discharge, and its lifetime is often long enough ($\gtrsim$100 ms) that a control system might have a realistic chance of acting to avoid an unintentional back transition.

ACKNOWLEDGMENTS

This material is based upon work supported by the U.S. Department of Energy, Office of Science, Office of Fusion Energy Sciences, using the DIII-D National Fusion Facility, a DOE Office of Science user facility, under Award Nos. DE-FG02-07ER54917, DE-FC02-04ER54698, DE-AC05-06OR23100, DE-FG02-89ER53296, and DE-AC02-09CH11466. DIII-D data shown in this paper can be obtained in digital format by following the links at https://fusion.gat.com/global/D3D_DMP.

APPENDIX A: SHEARING AND DECORRELATION RATE CALCULATIONS

1. Shearing rate calculations

The $E\times B$ rotation frequency is fit to the form developed by Burrell[31] and given by the following equation:

$$\omega_E = B + A_{in}\frac{(1+\alpha_{in}x_{in})e^{x_{in}} - e^{-x_{in}}}{e^{x_{in}} - e^{-x_{in}}} - A_{out}\frac{e^{x_{out}} - (1+\alpha_{out}x_{out})e^{-x_{out}}}{e^{x_{out}} - e^{-x_{out}}} \qquad \text{(A1)}$$

$$x_{in} = (\psi_{in} - \psi_N)/w_{in}, \quad x_{out} = (\psi_{out} - \psi_N)/w_{out}$$

where B, A_{in}, A_{out}, α_{in}, α_{out}, ψ_{in}, ψ_{out}, w_{in}, w_{out} are fit parameters. The result is then used to calculate $\omega_{E\times B}$ as described in the text in Eq. (2).

One of the vertical CER chords in the outer half of the E_r well was unavailable during this experiment, so one point is missing in the poloidal flow v_θ profile. However, toroidal flow v_ϕ, temperature T, and density are still available, and v_θ is very small and is not experiencing strong radial variation. Thus, the $v_\theta B_\phi$ term in Eq. (1) is about 10% of the $v_\phi B_\theta$ term across most of the profile and roughly 10% as large as the peak in the diamagnetic term (p'/Zen). Furthermore, radial variation in v_θ is comparable to the uncertainty in the measurements. Rather than discarding important and valid information about the other profiles, the missing point in v_θ is interpolated from its nearest neighbors and assigned double uncertainty (compared to interpolating from its neighbors' uncertainty). However, the term in question is so small that the extra uncertainty is difficult to discern when propagated into the final product.

2. Turbulence decorrelation rate calculations

The time delayed cross correlation $C(t_{delay})$ is calculated for a pair of chords, producing the red curve labeled "Correlation" shown in Fig. 18(a). The Hilbert envelope $\sqrt{y^2 + H(y)^2}$, where $H(y)$ is the Hilbert transform, of $C(t_{delay})$ is calculated (black curve above the red one) and the coordinates of the peak are recorded. The coordinates

from the peak correlations of several chord pairs with different vertical separations are fit to $C(t_{delay}) = C_{max}\,\mathrm{Exp}(-|t_{delay}\omega_T|)$, as seen in Fig. 18(b). This procedure measures the plasma frame decorrelation rate. Using the autocorrelation time (as could be calculated from the width of the envelope in Fig. 18(a)) gives the rate in the lab frame, which is unsuitable because it includes spatial decorrelation as eddies are advected past the BES chords by $E \times B$ drifts.[52] If this calculation is performed on the entire frequency range available from BES, a very low decorrelation rate is found due to the presence of the coherent MPM and its sidebands, which contribute significant power to the spectrum for $20 < f < 150$ kHz. As seen in Section IV, the MPM is localized like a ballooning mode, implying its parallel correlation length is a fraction of the poloidal circumference of the plasma. But the calculation of $\omega_{E\times B}$ is for flute like turbulence with very long parallel correlation length. So, the Hahm-Burrell model of shear suppression is not applicable to the MPM both because it is coherent rather than turbulent and also because its spatial correlation properties are ballooning-like rather than flute-like. Thus, the BES data are bandpass filtered to $150 \le f \le 450$ kHz before calculating ω_T ($f > 450$ kHz is noise).

APPENDIX B: CALCULATING PEAK FREQUENCY AND WAVENUMBER FROM CORRELATION FUNCTIONS

In order to measure the frequency f, wavenumber k, and lab-frame propagation velocity v_p of the mode in question, $\tilde{I}/I \propto \tilde{n}/n$ was computed for each chord in a column. Time delay cross correlation functions were calculated for each unique chord pair, excluding correlations of chords with themselves. The result, $C(t_{delay}, \Delta Z)$, where t_{delay} is the variable lag time and ΔZ is the spatial separation of the chords, was fit to

$$C(t_{delay}, \Delta Z) = C_{max}\cos(2\pi f t_{delay} - k\Delta Z) \times \mathrm{Exp}[-|t_{delay}/\tau_c|]\,\mathrm{Exp}[-|\Delta Z/\lambda_c|] \quad \text{(B1)}$$

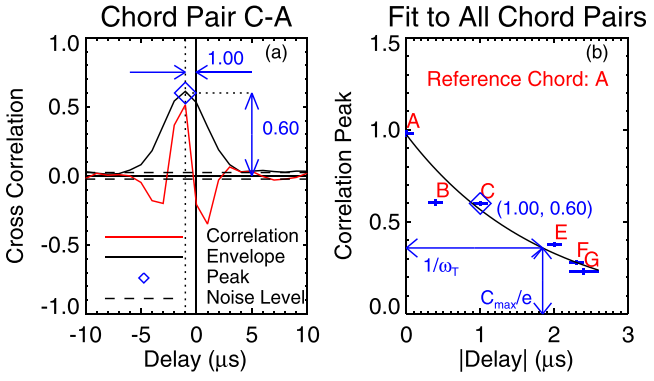

FIG. 18. Method of calculating decorrelation rate ω_T from BES data. (a) Cross correlation function (red) between two vertically separated chords with Hilbert envelope overlaid in black. The envelope peak is marked with a blue diamond and the peak envelope value and delay at this peak are measured by blue with arrows. (b) The peak from the left plot is plotted here along with similar measurements from other chord pairs; blue symbols with red labels. The point calculated from the left plot is marked with a diamond and coordinate label. The data are fit to $C(t_{delay}) = C_{max}\exp(-|t_{delay}\,\omega_T|)$ (black curve) and ω_T is recorded. Shot 154754 2370.0-2435.5 ms. Example uses BES column 6. For chord positions, see Fig. 4.

where C_{max} is the peak cross correlation, τ_c is the correlation time, and λ_c is the correlation length. The IDL MPFIT[53] implementation of the Levenberg-Marquardt algorithm for least squares minimization[54] was used. An example of this analysis is shown in Figure 19.

C_{max} may differ from 1 as random noise will prevent two separate chords from agreeing perfectly, even at arbitrarily close spacing. The value of τ_c obtained from the fit includes effects of decorrelation of the entire spectrum, not just the mode under investigation, as no frequency filtering was performed in this analysis. The correlation length λ_c is much longer than the physical array of BES chords and is probably not measured accurately beyond the statement that $\lambda_c \gg \max(\Delta Z) = 9.6$cm. Similarly, τ_c is often much longer than the time window chosen. This analysis was repeated for many sequential overlapping time windows to build a time history of $v_p = 2\pi f/k$ and other quantities. The data were not frequency filtered before this analysis because "the mode" strongly dominates the fit in Eq. (B1) and the frequency changes during the slowdown and the mode could escape the filtering window. A windowed Fourier transform was calculated and from this the mode amplitude at f was found at each time-slice. The result is qualitatively the same as averaging amplitude over a frequency range containing the mode and its sidebands, such as taking the average amplitude in $40 < f < 80$ kHz for each slice. The resulting histories are shown in Fig. 9 for a short time window just before the start of transition activity.

Some of the BES chords experience clipping or saturation during the hard back transition transients, but as the purpose of this analysis is to track the motion of "blobs," this should not be a serious problem as the photodiodes used by BES[55] do not appear to suffer long lasting systematic changes to their behavior after a saturation/clipping event (some light sensors do become nonlinear near saturation and also can draw enough current to heat themselves and change their gain with effects persisting after saturation has ended, but that turns out not to be a concern in this case). Indeed, it is clear from Fig. 8 and videos of BES fast intensity vs. R-Z that the v_p lock is not an artifact of clipping. Locking also occurs before the first type-III ELM in soft H-L sequences and in these cases, clipping is uncommon (because the change in density is not as great), and still the behavior is the same.

APPENDIX C: CALCULATION OF LOCAL WAVENUMBER

Local wavenumber k_{ij} may be calculated using the two point technique:[56]

$$G_{ij}(f) = F_i^* F_j$$
$$\phi_{ij}(f) = \mathrm{atan}\left(\frac{Im(G_{ij})}{Re(G_{ij})}\right) \quad \text{(C1)}$$
$$k_{ij}(f) = \frac{\phi_{ij}(f)}{Z_i - Z_j}$$

where F_i^* is the complex conjugate of the Fourier transform of the normalized $(\tilde{n}/n)$ signal from chord i, ϕ_{ij} is the phase delay between chords i and j limited to $-\pi < \phi < \pi$, and G_{ij}

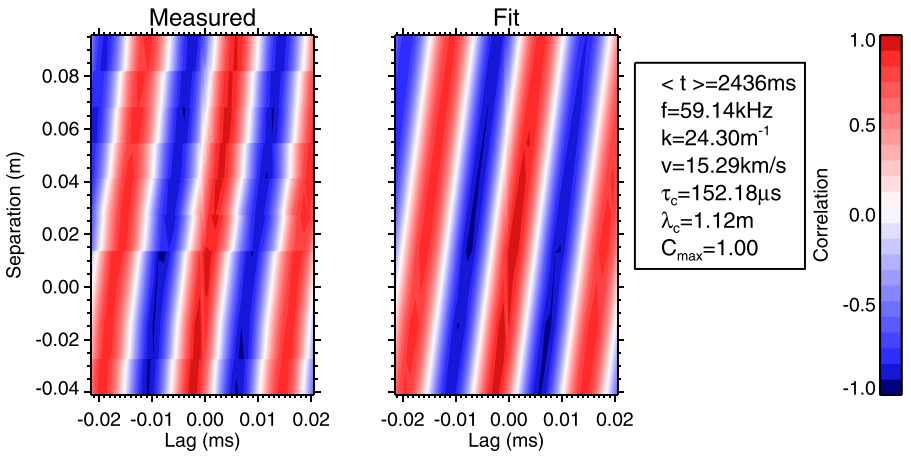

FIG. 19. Time delayed cross correlation functions from column 6 BES data (left) from an example time window centered around 2436 ms in shot 154754 are shown with a fit to $C_{max}\cos(2\pi f t_{lag} - k\Delta Z)\exp[-|t_{lag}/\tau_c|]\exp[-|\Delta Z/\lambda_c|]$ (right).

is the cross-power spectrum between the chords. This operation is repeated on all of the unique chord pairs in a column, excluding $i = j$. A dispersion diagram (Fig. 10) can be made from the histogram of k and f values, where the total power in each bin, rather than just the number of samples, is counted. While the method of fitting sinusoids to time delayed cross correlation functions was useful for identifying the characteristics of the dominant frequency component, this method reveals the behavior of k and v_p at different frequencies. In general, BES is not equally sensitive to all wavenumbers and a spatial transfer function can be used to correct the k spectrum. However, the transfer function is essentially flat[38] for $k_z < 1\,\mathrm{cm}^{-1}$, so no correction is needed when studying the MPM.

APPENDIX D: COORDINATE MAPPING UNCERTAINTIES IN DIII-D

Data from BES and Thomson Scattering (TS) are mapped to ψ_N using a simple equilibrium reconstruction (JT EFIT).[39] However, this is not perfect due to uncertainties in the positions of diagnostic chords, errors in the reconstruction due to 3D error fields, and finite lifetime of the excitation state of injected neutral atoms. The data in Fig. 11 have been corrected for alignment issues as follows: The foot of the T_e pedestal, as determined by a tanh fit,[21] is assumed to be at the separatrix and the Thomson profiles [Figs. 11(b) and 11(c)] are shifted outward by $2\%\psi_N$ to enforce this. The BES data [Fig. 11(a)] are shifted outward as well on the basis that excited beam ions have a finite lifetime and the delay between excitation and emission translates to an inward shift in position. The magnitude of this shift is expected to be about 0.66 cm (≈3 ns lifetime × 2.2 mm/ns for 50 keV beam energy),[38] which translates to about 2% in ψ_N. Absolute error in the measurements of the BES array's position[37] could be ≈5mm (because of the way the chords are secured in a common mounting bracket,[57] uncertainty in the relative positions between chords should be negligible).

[1]D. Eldon, R. L. Boivin, R. J. Groebner, T. H. Osborne, P. B. Snyder, A. D. Turnbull, J. A. Boedo, K. H. Burrell, E. Kolemen, L. Schmitz, G. R. Tynan, and H. R. Wilson, "Investigation of peeling-ballooning stability prior to transient outbursts accompanying transitions out of H-mode in DIII-D," Phys. Plasmas **22**, 052109 (2015).

[2]F. Wagner, G. Becker, K. Behringer, D. Campbell, A. Eberhagen, W. Engelhardt, G. Fussmann, O. Gehre, J. Gernhardt, G. v. Gierke, G. Haas, M. Huang, F. Karger, M. Keilhacker, O. Klüber, M. Kornherr, K. Lackner, G. Lisitano, G. G. Lister, H. M. Mayer, D. Meisel, E. R. Müller, H. Murmann, H. Niedermeyer, W. Poschenrieder, H. Rapp, H. Röhr, F. Schneider, G. Siller, E. Speth, A. Stäbler, K. H. Steuer, G. Venus, O. Vollmer, and Z. Yü, "Regime of improved confinement and high beta in neutral-beam-heated-divertor discharges of the ASDEX tokamak," Phys. Rev. Lett. **49**, 1408 (1982).

[3]K. H. Burrell, "Summary of experimental progress and suggestions for future work (H mode confinement)," Plasma Phys. Controlled Fusion **36**, A291 (1994).

[4]L. Schmitz, L. Zeng, T. L. Rhodes, J. C. Hillesheim, E. J. Doyle, R. J. Groebner, W. A. Peebles, K. H. Burrell, and G. Wang, "Role of zonal flow predator-prey oscillations in triggering the transition to H-Mode confinement," Phys. Rev. Lett. **108**, 155002 (2012).

[5]L. Schmitz, L. Zeng, T. L. Rhodes, J. C. Hillesheim, W. A. Peebles, R. J. Groebner, K. H. Burrell, G. R. McKee, Z. Yan, G. R. Tynan, P. H. Diamond, J. A. Boedo, E. J. Doyle, B. A. Grierson, C. Chrystal, M. E. Austin, W. M. Solomon, and G. Wang, "The role of zonal flows and predator-prey oscillations in triggering the formation of edge and core transport barriers," Nucl. Fusion **54**, 073012 (2014).

[6]T. H. Osborne, J. R. Ferron, R. J. Groebner, L. L. Lao, A. W. Leonard, M. A. Mahdavi, R. Maingi, R. L. Miller, A. D. Turnbull, M. Wade, and J. Watkins, "The effect of plasma shape on H-mode pedestal characteristics on DIII-D," Plasma Phys. Controlled Fusion **42**, A175 (2000).

[7]G. Federici, P. Andrew, P. Barabaschi, J. Brooks, R. Doerner, A. Geier, A. Herrmann, G. Janeschitz, K. Krieger, A. Kukushkin, A. Loarte, R. Neu, G. Saibene, M. Shimada, G. Strohmayer, and M. Sugihara, "Key ITER plasma edge and plasma-material interaction issues," J. Nucl. Mater. **313**, 11 (2003).

[8]A. Loarte, M. Sugihara, M. Shimada, A. Kukushkin, D. Campbell, M. Pick, C. Lowry, M. Merola, R. A. Pitts, V. Riccardo, G. Arnoux, W. Fundamenski, G. F. Matthews, S. Pinches, A. Kirk, E. Nardon, T. Eich, A. Herrmann, G. Pautasso, A. Kallenbach, G. Saibene, G. Federici, R. Sartori, G. Counsell, A. Portone, M. Cavinato, M. Lehnen, A. Huber, V. Philipps, D. Reiter, V. Kotov, R. Koslowski, G. Maddaluno, B. Lipschultz, D. Whyte, B. LaBombard, R. Granetz, A. W. Leonard, M. Fenstermacher, E. Hollman, P. C. Stangeby, M. Kobayashi, R. Albanese, G. Ambrosino, M. Ariola, G. de Tommasi, J. Gunn, M. Becoulet, L. Colas, M. Goniche, E. Faudot, and D. Milanesio, "Power and particle fluxes at the plasma edge of ITER: Specifications and physics basis," in Proceedings of the 22nd IAEA Fusion Energy Conference in Genevea, 2008.

[9]A. Loarte, G. Huijsmans, S. Futatani, L. R. Baylor, T. E. Evans, D. M. Orlov, O. Schmitz, M. Becoulet, P. Cahyna, Y. Gribov, A. Kavin, A. S. Naik, D. J. Campbell, T. Casper, E. Daly, H. Frerichs, A. Kischner, R. Laengner, S. Lisgo, R. A. Pitts, G. Saibene, and A. Wingen, "Progress on the application of ELM control schemes to ITER scenarios from the non-active phase to DT operation," Nucl. Fusion **54**, 033007 (2014).

[10]P. B. Snyder, H. R. Wilson, J. R. Ferron, L. L. Lao, A. W. Leonard, T. H. Osborne, A. D. Turnbull, D. Mossessian, M. Murakami, and X. Q. Xu, "Edge localized modes and the pedestal: A model based on coupled peeling-ballooning modes," Phys. Plasmas **9**, 2037 (2002).

[11]H. R. Wilson, P. B. Snyder, G. T. A. Huysmans, and R. L. Miller, "Numerical studies of edge localized instabilities in tokamaks," Phys. Plasmas **9**, 1277 (2002).
[12]A. Loarte, G. Saibene, R. Sartori, D. Campbell, M. Becoulet, L. Horton, T. Eich, A. Herrmann, G. Matthews, N. Asakura, A. Chankin, A. Leonard, G. Porter, G. Federici, G. Janeschitz, M. Shimada, and M. Sugihara, "Characteristics of type I ELM energy and particle losses in existing devices and their extrapolation to ITER," Plasma Phys. Controlled Fusion **45**, 1549 (2003).
[13]T. E. Evans, R. A. Moyer, J. G. Watkins, T. H. Osborne, P. R. Thomas, M. Becoulet, J. A. Boedo, E. J. Doyle, M. E. Fenstermacher, K. H. Finken, R. J. Groebner, M. Groth, J. H. Harris, G. L. Jackson, R. J. L. Haye, C. J. Lasnier, S. Masuzaki, N. Ohyabu, D. G. Pretty, H. Reimerdes, T. L. Rhodes, D. L. Rudakov, M. J. Schaffer, M. R. Wade, G. Wang, W. P. West, and L. Zeng, "Suppression of large edge localized modes with edge resonant magnetic fields in high confinement DIII-D plasmas," Nucl. Fusion **45**, 595 (2005).
[14]E.-J. Kim and P. H. Diamond, "Zonal flows and transient dynamics of the L-H transition," Phys. Rev. Lett. **90**, 185006 (2003).
[15]K. Miki, P. H. Diamond, Ö. D. Gürcan, G. R. Tynan, T. Estrada, L. Schmitz, and G. S. Xu, "Spatio-temporal evolution of the L→I→H transition," Phys. Plasmas **19**, 092306 (2012).
[16]K. Miki, P. H. Diamond, L. Schmitz, D. C. McDonald, T. Estrada, Ö. D. Gürcan, and G. R. Tynan, "Spatio-temporal evolution of the H→L back transition," Phys. Plasmas **20**, 062304 (2013).
[17]J. L. Luxon, "A design retrospective of the DIII-D tokamak," Nucl. Fusion **42**, 614 (2002).
[18]. D. N. Hill and the DIII-D Team, "DIII-D research towards resolving key issues for ITER and steady-state tokamaks," Nucl. Fusion **53**, 104001 (2013).
[19]G. McKee, R. Ashley, R. Durst, R. Fonk, M. Jakubowski, K. Tritz, K. Burrell, C. Greenfield, and J. Robinson, "The beam emission spectroscopy diagnostic on the DIII-D tokamak," Rev. Sci. Instrum. **70**, 913 (1999).
[20]K. H. Burrell, P. Gohil, R. J. Groebner, D. H. Kaplan, J. I. Robinson, and W. M. Solomon, "Improved charge-coupled device detectors for high-speed, charge exchange spectrscopy studies on the DIII-D tokamak," Rev. Sci. Instrum. **75**, 3455 (2004).
[21]R. J. Groebner, D. R. Baker, K. H. Burrell, T. N. Carlstrom, J. R. Ferron, P. Gohil, L. L. Lao, T. H. Osborne, D. M. Thomas, W. P. West, J. A. Boedo, R. A. Moyer, G. R. McKee, R. D. Deranian, E. J. Doyle, C. L. Rettig, T. L. Rhodes, and J. C. Rost, "Progress in quantifying the edge physics of the H mode regime in DIII-D," Nucl. Fusion **41**, 1789 (2001).
[22]D. Eldon, B. D. Bray, T. M. Deterly, C. Liu, M. Watkins, R. J. Groebner, A. W. Leonard, T. H. Osborne, P. B. Snyder, R. L. Boivin, and G. R. Tynan, "Initial results of the high resolution edge Thomson scattering upgrade at DIII-D," Rev. Sci. Instrum. **83**, 10E343 (2012).
[23]H. Biglari, P. H. Diamond, and P. W. Terry, "Influence of sheared poloidal rotation on edge turbulence," Phys. Fluids. B **2**, 1 (1990).
[24]T. S. Hahm, "Rotation shear induced fluctuation decorrelation in a toroidal plasma," Phys. Plasmas **1**, 2940 (1994).
[25]T. S. Hahm and K. H. Burrell, "Flow shear induced fluctuation suppression in finite aspect ratio shaped tokamak plasma," Phys. Plasmas **2**, 1648 (1995).
[26]T. S. Hahm and K. H. Burrell, "ExB flow shear effects on radial correlation length of turbulence and gyroradius scaling of confinement," Phys. Plasmas **3**, 427 (1996).
[27]K. H. Burrell, "Effects of E×B velocity shear and magnetic shear on turbulence and transport in magnetic confinement devices," Phys. Plasmas **4**, 1499 (1997).
[28]O. D. Gürcan, "Effect of sheared flow on the growth rate and turbulence decorrelation," Phys. Rev. Lett. **109**, 155006 (2012).
[29]G. R. Tynan, M. Xu, P. H. Diamond, J. A. Boedo, I. Cziegler, N. Fedorczak, P. Manz, K. Miki, S. Thakur, L. Schmitz, L. Zeng, E. Doyle, G. M. McKee, Z. Yan, G. S. Xu, B. N. Wan, H. Q. Wang, H. Y. Guo, J. Dong, K. Zhao, J. Cheng, W. Y. Hong, and L. W. Yan, "Turbulent-driven low-frequency sheared E×B flows as the trigger for the H-mode transition," Nucl. Fusion **53**, 073053 (2013).
[30]I. Cziegler, G. R. Tynan, P. H. Diamond, A. E. Hubbard, J. W. Hughes, J. Irby, and J. L. Terry, "Zonal flow production in the L-H transition in Alcator C-Mod," Plasma Phys. Controlled Fusion **56**, 075013 (2014).
[31]K. H. Burrell, "Fitting function for characterization of the edge E_r well in H-mode plasmas," (unpublished).
[32]J. C. Hillesheim, W. A. Peebles, T. L. Rhodes, L. Schmitz, A. E. White, and T. A. Carter, "New plasma measurements with a multichannel millimeter-wave fluctuation diagnostic system in the DIII-D tokamak," Rev. Sci. Instrum. **81**, 10D907 (2010).
[33]C. M. Muscatello, C. W. Domier, X. Hu, G. J. Kramer, N. C. Luhmann, Jr., X. Ren, P. Riemenschneider, A. Spear, B. J. Tobias, E. Valeo, and L. Yu, "Technical overview of the millimeter-wave imaging reflectometer on the DIII-D tokamak," Rev. Sci. Instrum. **85**, 11D702 (2014).
[34]M. A. Van Zeeland, R. L. Boivin, T. N. Carlstrom, T. Deterly, and D. K. Finkenthal, "Fiber optic two-color vibration compensated interferometer for plasma density measurements," Rev. Sci. Instrum. **77**, 10F325 (2006).
[35]M. E. Austin and J. Lohr, "Electron cyclotron emission radiometer upgrade on the DIII-D tokamak," Rev. Sci. Instrum. **74**, 1457 (2003).
[36]J. D. King, E. J. Strait, R. L. Boivin, D. Taussig, M. G. Watkins, J. M. Hanson, N. C. Logan, C. Paz-Soldan, D. C. Pace, D. Shiraki, M. J. Lanctot, R. J. La Haye, L. L. Lao, D. J. Battaglia, A. C. Sontag, S. R. Haskey, and J. G. Bak, "An upgrade of the magnetic diagnostic system of the DIII-D tokamak for non-axisymmetric measurements," Rev. Sci. Instrum. **85**, 083503 (2014).
[37]W. M. Solomon, K. H. Burrell, P. Gohil, R. Groebner, and D. Kaplan, "Cross-calibrating spatial positions of light-viewing diagnostics using plasma edge sweeps in DIII-D," Rev. Sci. Instrum. **74**, 5084 (2003).
[38]M. W. Shafer, R. J. Fonk, G. R. Mckee, and D. J. Schlossberg, "Spatial transfer function for the beam emission spectroscopy diagnostic on DIII-D," Rev. Sci. Instrum. **77**, 10F110 (2006).
[39]L. L. Lao, H. S. John, R. D. Stambauh, A. G. Kellman, and W. Pfeiffer, "Reconstruction of current profile parameters and plasma shapes in tokamaks," Nucl. Fusion **25**, 1611 (1985).
[40]G. Bateman and D. B. Nelson, "Resistive-ballooning-mode equation," Phys. Rev. Lett. **41**, 1804 (1978).
[41]N. M. Ferraro, S. C. Jardin, and P. B. Snyder, "Ideal and resistive edge stability calculations with M3D-C^1," Phys. Plasmas **17**, 102508 (2010).
[42]B. I. Cohen, M. V. Umansky, W. M. Nevins, M. A. Makowski, J. A. Boedo, D. L. Rudakov, G. R. McKee, Z. Yan, and R. J. Groebner, "Simulations of drift resistive ballooning L-mode turbulence in the edge plasma of the DIII-D tokamak," Phys. Plasmas **20**, 055906 (2013).
[43]M. S. Chu and M. Okabayashi, "Stabilization of the external kink and the resistive wall mode," Plasma Phys. Controlled Fusion **52**, 123001 (2010).
[44]E. J. Strait, T. S. Taylor, A. D. Turnbull, J. R. Ferron, L. L. Lao, B. Rice, O. Sauter, S. J. Thomson, and D. Wróblewski, "Wall stabilization of high beta tokamak discharges in DIII-D," Phys. Rev. Lett. **74**, 2483 (1995).
[45]M. Okabayashi, J. Bialek, A. Bondeson, M. S. Chance, M. S. Chu, A. M. Garofalo, R. Hatcher, Y. In, G. L. Jackson, R. J. Jayakumar, T. H. Jensen, O. Katsuro-Hopkins, R. J. La Haye, Y. Q. Liu, G. A. Navratil, H. Reimerdes, J. T. Scoville, E. J. Strait, M. Takechi, A. D. Turnbull, P. Gohil, J. S. Kim, M. A. Makowski, J. Manickam, and J. Menard, "Control of the resistive wall mode with internal coils in the DIII-D tokamak," Nucl. Fusion **45**, 1715 (2005).
[46]P. H. Rutherford, "Nonlinear growth of the tearing mode," Phys. Fluids **16**, 1903 (1973).
[47]J. A. Wesson, "Hydromagnetic stability of tokamaks," Nucl. Fusion **18**, 87 (1978).
[48]D. A. Humphreys, J. R. Ferron, R. J. La Haye, T. C. Luce, C. C. Petty, R. Prater, and A. S. Welander, "Active control for stabilization of neoclassical tearing modes," Phys. Plasmas **13**, 056113 (2006).
[49]J. D. Huba, *NRL Plasma Formulary* (Naval Research Laboratory, Washington, D.C., 2009), pp. 19, 28–29.
[50]B. D. Dudson, M. V. Umansky, X. Q. Xu, P. B. Snyder, and H. R. Wilson, "BOUT++: A framework for parallel plasma fluid simulations," Comput. Phys. Commun. **180**, 1467 (2009).
[51]A. D. Turnbull, L. L. Lao, T. H. Osborne, O. Sauter, E. J. Strait, T. S. Taylor, M. S. Chu, J. R. Ferron, C. M. Greenfield, A. W. Leonard, R. L. Miller, P. B. Snyder, H. R. Wilson, and H. Zohm, "Edge localized modes in DIII-D high performance discharges," Plasma Phys. Controlled Fusion **45**, 1845 (2003).
[52]G. R. McKee, R. J. Fonk, D. K. Gupta, D. J. Schlossberg, M. W. Shafer, R. L. Boivin, and W. Solomon, "Plasma turbulence imaging via beam emission spectroscopy in the core of the DIII-D tokamak," Plasma Fusion Res. **2**, S1025 (2007).
[53]C. B. Markwardt, "Non-linear least squares fitting in IDL with MPFIT," in *Astronomical Data Analysis Software and Systems XVIII ASP Conference Series* (Astronomical Society of the Pacific, 2009), Vol. 411, p. 251.

[54]D. W. Marquardt, "An algorithm for least-squares estimation of nonlinear parameters," J. Soc. Ind. Appl. Math. **11**, 431 (1963).
[55]G. R. McKee, R. J. Fonck, D. K. Gupta, D. J. Schlossberg, M. W. Shafer, and R. L. Boivin, "High sensitivity beam emission spectroscopy for core plasma turbulence imaging," Rev. Sci. Instrum. **77**, 10F104 (2006).
[56]J. M. Beall, Y. C. Kim, and E. J. Powers, "Estimation of wavenumber and frequency spectra using fixed probe pairs," J. Appl. Phys. **53**, 3933 (1982).
[57]G. McKee, R. Ashley, R. Durst, R. Fonck, M. Jakubowski, K. Tritz, K. H. Burrell, C. M. Greenfield, and J. Robinson, "Beam emission spectroscopy diagnostic on the DIII-D tokamak," paper presented at the 12th High Temperature Plasma Diagnostics Conference in Princeton, NJ, 1998.